Synthetic Metals 287 (2022) 117056

Contents lists available at ScienceDirect

Synthetic Metals

journal homepage: www.elsevier.com/locate/synmet

Charge transport in cove-type graphene nanoribbons: The role of quasiparticles

Tiago de Sousa Araújo Cassiano [a], Leonardo Evaristo de Sousa [b,*], Luiz Antônio Ribeiro Junior [a], Geraldo Magela e Silva [a], Pedro Henrique de Oliveira Neto [a]

[a] Institute of Physics, University of Brasilia, 70919-970 Brasilia, Brazil
[b] Department of Energy Conversion and Storage, Technical University of Denmark, Denmark

ARTICLE INFO

Keywords:
SSH
Graphene
Polarons
Bipolarons
Charge transport
GNR

ABSTRACT

Previous reports indicate that cove-type graphene nanoribbons (CGNR) may present high intrinsic charge mobility of almost 15,000 cm^2/Vs. Still, with experimental estimates varying from 150 to 15,000 cm^2/Vs. Typically, theoretical mobilities are obtained from methods such as the Drude-Smith model, which tends to neglect the electron-phonon coupling mechanism, or the Boltzmann transport equation, that considers only acoustic phonons. As such, more thorough approaches are needed. In this work, we simulated charge transport in 4-CGNR by explicitly contemplating the lattice collective behavior. The nanoribbon is simulated by a two-dimensional Su-Schrieffer-Heeger (SSH) tight-binding model with electron-phonon coupling and considering all phonon modes. Results show the rise of two quasiparticles: polaron and bipolaron. We probed their dynamical properties by including the presence of an external electric field. Findings indicate that each carrier has a characteristic transport regime that is deeply related to phonon collision interactions. Model derived mobilities for polarons and bipolarons reach up to 18,000 cm^2/Vs and 1500 cm^2/Vs, respectively. Furthermore, calculations reveal the carriers to be highly efficient charge transporters, with a field independent low effective mass and notable mobility, delivering a better performance than other narrow GNRs. All presented features place the CGNR as a potential base material of future high-quality organic-based optoelectronic devices. The work also contributes to the theoretical understanding of transport physics in highly confined materials.

1. Introduction

Since its isolation in 2004 [1], graphene is playing a decisive role in material sciences due to its remarkable transport properties [2]. Currently, this carbon allotrope participates in numerous technological and scientific breakthroughs [3–6]. Most of the attention regarding graphene relates to its unique linear band structure. This topological feature allows charge carriers with exceptional mobility up to 200,000 cm^2/Vs [7,8]. Regardless of the numerous advantages, graphene presents no electronic bandgap. This setback prevents its use in optoelectronics. In this context, a viable gap opening strategy relies on reducing the graphene dimensionality. Known as graphene nanoribbon (GNR) [9,10], this nanostructure may allow a non-zero gap due to quantum confinement effects. In addition, simple geometry adjustments can regulate its electronic properties. Controlling structural characteristics such as the width [9] or the edge shape [11,12] frequently leads to tunable electronic and transport properties. These features, allied with recent synthesis advances, turn the GNRs into a promising material class for future optoelectronics.

Recently, a report described the route synthesis of a well-defined GNR synthesized in a bottom-up liquid-based process [13]. Experimental evidence suggests that cove-type graphene nanoribbons (CGNR) possess a set of physical attributes that overcome previous synthesized GNRs. Unlike many GNRs syntheses [14–16], the one applied for the CGNR delivers extremely long specimens with almost no defects. Moreover, the bottom-up procedure, along with the liquid-based feature, is particularly desired for large-scale production. Physical measurements also reveal the nanoribbon applicability potential. The UV–vis spectrum indicates an optical bandgap of 1.88 eV [13], which is suitable for semiconducting applications. Also, time-resolved terahertz (THz) conductivity measurements suggest the presence of charge carriers with excellent intramolecular mobilities estimated between 150 and 15,000 cm^2/Vs [13].

To make sense of these results, a detailed description of charge

* Corresponding author.
E-mail address: ledso@dtu.dk (L.E. de Sousa).

https://doi.org/10.1016/j.synthmet.2022.117056
Received 13 January 2022; Received in revised form 8 March 2022; Accepted 10 March 2022
Available online 17 March 2022

transport in CGNR is imperative. It is well-established that low-dimensional organic semiconductors present local distortion with self-trapped charged states, forming quasiparticles. These very structures are the result of collective behavior that entangles both the lattice and charges. Each type of quasiparticle has characteristic values of charge and spin. Furthermore, their existence links to electronic intragap states. In particular, charged quasiparticles play a lead role as carriers in the transport of charge. Here, two quasiparticles have a notorious relevance: the polaron and the bipolaron [17]. The first carrier is a polarized region with charge $\mp e$ and half spin. The latter is a bound state of polarons, being spinless with charge $\mp 2e$. An adequate physical description of the charge transport requires the knowledge of these structures' behavior [18–21].

Theoretical approaches based on DFT, tight-binding, and others methods were forged to investigate charge transport in graphene-based materials [22–25,26,27]. In almost every case, the studies center on characterizing the electronic structure of the materials, using models to translate parameters such as effective mass into mobility estimates. These models include the Boltzmann transport equation (BTE)[28] and the Drude-Smith (DS) model[29]. The DS model bears some limitations despite its relative success over the past two decades [30]. Although it accounts for charge localization [31], the carrier's quasiparticle nature is suppressed. This accuracy loss might reduce the model suitability in quantum-confined materials. As to the BTE model, it neglects the role of optical phonons, potentially underestimating lattice effects. In that sense, recently, we reported an alternative way to probe electronic transport explicitly considering collective behavior in GNRs [32] by combining non-adiabatic simulations with classical trajectory dynamics. The study focused on the so-called armchair graphene nanoribbons (AGNRs) and comparison with theoretical and experimental works showed good agreement. Hence, the quasiparticle treatment we propose here should deliver a better representation of the charge transport mechanism in 4-CGNR, as it suffers from neither limitation. In addition, transport phenomena in other nanoribbons have been shown to be mainly quasiparticle-mediated[9,18–20], suggesting that BTE and DS-based approaches supported by DFT may not be completely adequate for these materials as well.

In the present work, we investigated charge transport in the 4-CGNR by characterizing the charged quasiparticles under the influence of an electric field. Our model consists of an extended two-dimensional Su-Schrieffer-Heeger (SSH) model Hamiltonian [33]. Charged states revealed the presence of two charged quasiparticles in the 4-CGNR: a polaron and a bipolaron. Results showed that each polarized region presents a distinctive transport regime. The profiles are a result of the interaction between the carriers and scattered phonons, which can be better appreciated in terms of a quasiparticle picture. In that sense, the importance of methods that account for the collective behavior became visible. These approaches are more likely to offer a better physical description in such confined systems. Finally, we extracted significant low effective masses for both carriers. We also carried out further characterization by estimating the I-V curve and the dispersion coefficient of each polarized region. Altogether, these properties corroborate experimental evidence that suggests highly efficient charge carriers in 4-CGNR, reinforcing this material's place as a strong candidate in future optoelectronics.

2. Methodology

We model the 4-CGNR through a two-dimensional extended SSH model with electron-phonon coupling. Fig. 1 shows a representation of this nanoribbon. The indexation adopted is presented as well. Past works describe in detail the model usage [19–21,34,35]. In summary, the

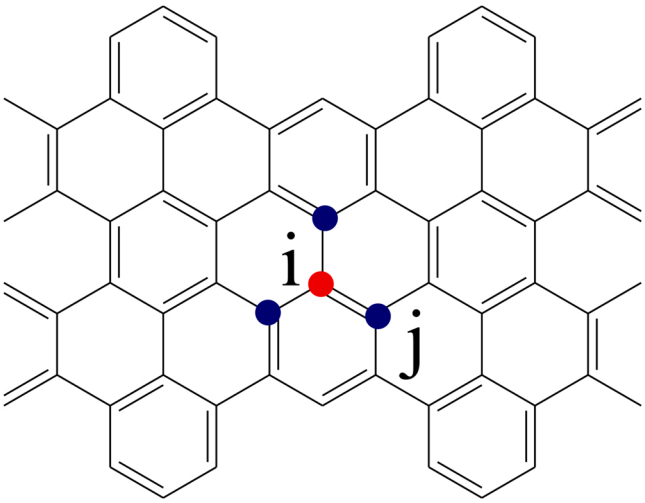

Fig. 1. Diagram of the 4-CGNR [11,13,28]. The site's indexation is illustrated. The red dot represents the *i*-th site. The blue colored sites are their nearest neighbors.

modeling splits the nanoribbon's physical description into two parts that should be solved simultaneously: an electronic (H_{tb}) and a lattice term (H_{latt}). We treat the first part quantum mechanically through a tight-binding like Hamiltonian for the π-electrons. On the other hand, the description of the latter lies in a classical framework. Then, writing the first part of the hybrid Hamiltonian (H) in the second quantization formalism,

$$H_{tb} = -\sum_{<i,j>,s} [t_{i,j} C^{\dagger}_{i,s} C_{j,s} + h.c.]. \tag{1}$$

Here, $C^{\dagger}_{i,s}$ is the creation operator for a π-electron with spin s in the i-th site. Accordingly, the operator $C_{j,s}$ annihilates a π-electron with spin s in the j-th site. $t_{i,j}$ is the hopping integral, and the brackets in the summation represent a pair-wise sum. The distortion amplitude in σ-bonds amounts to about 2% [36] of the total length in GNRs. Thus, expanding the hopping integral around the undisturbed length [33] gives

$$t_{i,j} = t_0 + \alpha \eta_{i,j}. \tag{2}$$

t_0 is the hopping integral of the symmetric lattice, $\eta_{i,j}$ the relative displacement of the bond between the i-th and j-th sites, and α is the electron-phonon constant. This last term connects the electronic phenomena, mediated by the π-electrons, with the lattice structural disorder. We emphasize that Equation 2 inserts a local dependence into the hopping integral. Then, unlike pure tight-binding approaches, this model allows a positional sensibility in the charge transport process.

As previously mentioned, our description lies under the approximation of small oscillations. This allows us to model the lattice term, H_{latt}, based on the harmonic approximation,

$$H_{latt} = \frac{K}{2}\sum_{<i,j>} \eta^2_{i,j} + \frac{1}{2M}\sum_i P^2_i. \tag{3}$$

K is the elastic constant of the σ bonds, M the site's mass, and P_i is the conjugated momentum operator.

We start solving the hybrid Hamiltonian in its stationary form ($P_i = 0$). To numerically evaluate it, one must first find the set $\{\eta_{i,j}\}$. Starting from an initial guess, we can diagonalize the electronic Hamiltonian. Then, the set of eigenstates and eigenvalues are used to update $\{\eta_{i,j}\}$. Following the Ehrenfest theorem, the site coordinates ($\{q_i\}$) are

determined by the Euler-Lagrange equations. With $\langle L\rangle$ the expected value of the Lagrangian, we have,

$$\frac{d}{dt}\left(\frac{\partial\langle L\rangle}{\partial\dot{q}_i}\right)=\frac{\partial\langle L\rangle}{\partial q_i}. \tag{4}$$

$\langle L\rangle$ is calculated with a Slater-type wave function $|\psi\rangle$ of the occupied π-electrons. The solving of Equation 4 returns a new set of $\{\eta_{i,j}\}$. Based on the convergence criterion, this set is accepted if it is close enough to the previous one. Otherwise, we use the newly found $\{\eta_{i,j}\}$ to solve the electronic Hamiltonian once again. The whole process repeats until a stationary configuration arises. Our main objective in this work is to investigate charge transport in the 4-CGNR. For this purpose, we will first derive charged stationary solutions. These states are prepared by unbalancing the nanoribbon's total charge.

Next, we proceed to evolve the stationary states with time. To do so, we include the presence of an external electric field with a slowing varying potential vector $\mathbf{A}(t)$. Where $\mathbf{E}(t) = -(1/c)\dot{\mathbf{A}}(t)$. The Periels substitution transforms the hopping integral into [20,36].

$$t_{i,j}=e^{-i\gamma A_{i,j}}(t_0+\alpha\eta_{i,j}), \tag{5}$$

where $A_{i,j}$ is the projection of $\mathbf{A}(t)$ along the σ-bond that connects sites i and j. $\gamma = ea/(\hbar c)$, in which e is the elementary charge, a the lattice parameter and c the speed of light.

The evolution process consists of solving the time-dependent Schrodinger equation for the electronic part and Euler-Lagrange equations for the lattice. With $\{\psi_{k,s}\}$ the eigenvectors of the electronic Hamiltonian, Eq. (4) gives the following equation of motion:

$$\begin{aligned}F_{i,j}(t) &= M\ddot{\eta}_{i,j}=\frac{K}{2}(\eta_{i,i'}+\eta_{i,i''}+\eta_{j,j''}+\eta_{j,j'}-4\eta_{i,j})\\ &+\frac{\alpha}{2}(B_{i,i'}+B_{i,i''}+B_{j,j'}+B_{j,j''}-4B_{i,j}+c.c.),\end{aligned} \tag{6}$$

where,

$$B_{i,j}\equiv e^{-i\gamma A_{i,j}}\sum_{k,s}{}'\psi^*_{k,s}(i,t)\psi_{k,s}(j,t). \tag{7}$$

In Eq. (6), the prime on the site's index represents its firsts neighbors. The prime in Eq. (7) means a sum over the occupied orbitals. One can notice the explicit coupling between lattice and electronic phenomena by the terms that accompany α in Eq. (6) [34]. This equation governs the lattice time evolution.

The states $\{\psi_{k,s}\}$ evolve in time according to Schrodinger equation. Then,

$$i\hbar\frac{\partial}{\partial t}|\psi_k(t)\rangle = H|\psi_k(t)\rangle,$$

or,

$$|\psi_k(t+dt)\rangle = e^{-iH(t)dt/\hbar}|\psi_k(t)\rangle. \tag{8}$$

Let $\{|\phi_l(t)\rangle\}$ and $\{\epsilon_l\}$ be, respectively, the eigenvector and the eigenvalue sets of the electronic Hamiltonian at time t. Expanding the state over this basis gives

$$|\psi_k(t+dt)>=\sum_l\langle\phi_l(t)|\psi_k(t)\rangle e^{-ie_l dt/\hbar}|\phi_l(t)>. \tag{9}$$

Here, we emphasize that after each time step, dt, the set $\{\eta_{i,j}\}$ changes as well. Then, further time increment will require additional diagonalization and the re-utilization of Eqs. (8) and (6).

The electric field is included in a adiabatic manner by [19,34,36].

$$\mathbf{A}(t)=\begin{cases}0 & \text{if } t<0\\ -c\mathbf{E}_0(t-(\sin\frac{\pi}{\tau t})(\tau/\pi)) & \text{if } 0\le t<\tau,\\ -c\mathbf{E}_0(t-\tau/2) & \text{if } t\ge\tau \text{ and } t<t_{off}.\end{cases} \tag{10}$$

Here, parameter τ is the time required to achieve a regime of constant electric field, while t_{off} is the time when the field is shutdown.

Finally, we describe our probing method for the transport phenomenon of charge carriers in GNRs. All charged quasiparticles have, to some extent, a local charge spreading. In special, a stable carrier maintains its profile as time evolves. Thus, one can associate this structure with the center of the charge density. By doing that, the dynamics of the carrier turn into a projectile trajectory. Here, we model this motion by including Stokes dissipation model [32]. The equation of motion modeled becomes

$$F_X = M_{eff}\ddot{X} = qE_0 - Bv_X, \tag{11}$$

where M_{eff} is the quasiparticle effective mass, F_X the force experienced by the particle, B the dissipation coefficient, q the carrier's charge and v_X the velocity along the applied field direction. The solution of this differential equation gives the following trajectory [32]:

$$X(t) = X_0 + v_t t + \frac{v_0 - v_t}{k}(1-e^{-kt}), \tag{12}$$

in which X_0, and v_0 are, respectively, the particle position and velocity when the field becomes constant. v_t is the terminal velocity and k is a constant equals to B/m_{eff}. Fitting Eq. (12) returns v_t and k. A simple manipulation of both parameters also gives M_{eff} and B. In possession of these values, we are now able to characterize the charge carrier motion. The mobility (μ) can be estimated as:

$$\mu = v_t/\mathrm{E}_0. \tag{13}$$

Having v_t for a giving electric field strength also allows us to evaluate the quasiparticle current (I) and voltage (V). Let Q be the carrier's charge. Assuming a steady velocity regime, the current reads

$$I = \frac{Qv_t}{L_0}, \tag{14}$$

where L_0 is the length of the unit cell simulated. Accordingly, one can also estimate the potential under the regime of constant $\mathbf{E}$. If L_{exp} is the nanoribbon length and N_{cells} the integer number of unit cells in it, then, the potential reads

$$V = E_0 N_{cells} L_0. \tag{15}$$

Throughout this work, all parameters of the hybrid Hamiltonian are set based on previous works. $t_0 = 2.7$ eV [37], $K = 21$ eV/Å^2 [38] and $a = 1.41$ Å. Recently, we had estimated 4-CGNR's α at 4.6 eV/Å [11]. As for the parameters related with $\mathbf{A}(t)$, $\tau = 5\%t_{off}$, and t_{off} equals to the entire simulation time, which ranges between 400 and 500 fs. Finally, the experimental report of the 4-CGNR synthesis points out nanoribbons with about 200 nm in extension [13]. Therefore, we set $L_{exp} = 200$ nm. $N_{cells}L_0 = 189$ nm, and 191 nm for the polaron and bipolaron, respectively.

As a final remark, we must stress that the described model physically treats the dynamics of quasiparticles with opposite charges equally. Then, any transport probing of a positively charged carrier will extend to the negative case.

3. Results

Fig. 2 presents the 4-CGNR electronic response for charged configurations. Fig. 2(a)-(c) show the electronic energy levels close to the highest occupied molecular orbital (HOMO) for the neutral state, singly and doubly positively charged states. Each line represents an electronic state that a π-electron could access. As previously discussed, quasiparticles are associated with intragap states. The difference between these energy levels is also a way to characterize the carriers. The red line in (b) refers to the inferior orbital of the polaron's intragap. On the other hand, the blue line in (c) is this state for the bipolaron. One can notice that the

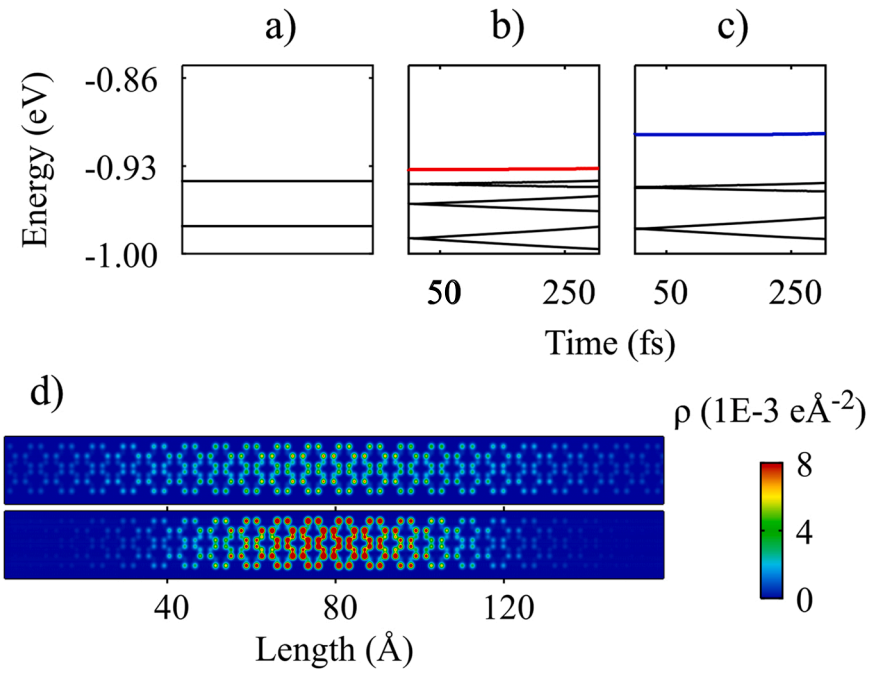

Fig. 2. The 4CGNR electronic profile: (a), (b) and (c) display, respectively, the electronic spectrum around the HOMO for the neutral, single, and doubly charged states. The red line indicates the intragap state associated with the polaron, while the blue line refers to the bipolaron. (d) shows the charge density (ρ) profiles of the charged states converged via the self-consistent approach. The upper nanoribbon refers to the prepared state with − 1 electron, while the lower one has − 2 electrons. Both profiles indicate clear charge localization. The former is the polaron and the latter the bipolaron.

state in (c) is more detached from the valence band than in (b). That is because the additional charge inserts further energetic distress in the material. As a result, bipolaron's intragap state becomes narrower than the polaron's.

Two polarized regions are associated with the charged stationary states. Figure 2(d) displays the charge density profile of the 4-CGNR positively charged. The colors symbolize the charge accumulation degree. Hot and cold tones indicate high and low charge density, respectively. The upper polarized region results from the removal of one electron. On the other hand, the lower heatmap shows a quasiparticle that accumulates a net charge of 2e. We recognize the upper polarized region as the polaron and the lower as the bipolaron.

A fact easily noted is that the polaron is wider than the bipolaron. We estimate the former's width to be 144 Å, while the latter's equals 100 Å, representing less than 10% of L_0. Naturally, this is a manifestation of the carrier localization property, which makes its structure occupy only a fraction of the system's extension. The reason for such discrepancy between the lengths lies in the inherent malleability of organic materials. Bipolaron posses more charge, which leads to stronger lattice deformations. Consequently, the polarized region becomes more concentrated. Nonetheless, our simulations indicate that 4-CGNR may host at least two types of polarized quasiparticles by unit cell. Their characteristics and properties should crucially influence the description of charge transport in that material.

We have analyzed the quasiparticles performance under the influence of electric fields in Fig. 3. The Fig. 3(a) and 3(b) show charge density snapshots of polaron and bipolaron states, respectively. In both cases, collective behavior is apparent. The first snap shows the charge density of the stationary state. Here, we can observe two localized charge accumulations. When time increases, these quasiparticles drift along the field direction, maintaining their characteristic shape. This consistent feature remains for all simulations in this work. Qualitatively, both carriers evolve in time similarly. At the time interval of 0–66 fs, there is no appreciable motion. That happens because, during this period, the electric field supports charge localization. Ultimately, this process increases the quasiparticle stability. Shortly after, the carrier has enough impulse to start drifting. Then, the charged structure enters into a regime of velocity gain. That state remains until, eventually, the quasiparticle reaches a maximum velocity. Previous works yield similar trajectories [20,32,39–41].

We emphasize that the velocity gain is not the same for both quasiparticles. Starting about the same position, after 313 fs, the polaron covers almost 100 Å, while the bipolaron reaches only 25 Å. That indicates that bipolaron offers more transport inertia than polaron. Such a characteristic is expected since bipolarons originate from a more intense lattice distortion. The charge density profile behaves collectively throughout the entire simulation time. Moreover, both polarized regions remained unchanged under external electric field, reinforcing their stability status.

Fig. 3(c) and 3(d) show, respectively, polaron and bipolaron trajectories under several electric field magnitudes. Each figure contains two graphs. The upper one displays the quasiparticle position as a function of time. On the other hand, below each position graph, we have the time evolution of velocity. The line colors address the field strength. Blue, red, and green colored plots refer to dynamics under the field values of 1210, 1820, and 3280 V/cm, respectively. As can be readily seen, all position graphs share a similar pattern. A regime of slow motion goes until about 200 fs. During this time, the quasiparticles are in a mobilization process, as discusses previously. Soon after, they begin to cover a substantial distance at a fast pace. This new stage is expected to endure while the electric field is present. Increasing the field strength leads to a predictable consequence: the quasiparticles are accelerated faster. That happens because the electric field is the source of energy.

Numerically, the quasiparticles respond differently to the external electric field. Despite that, their velocity plots have a similar shape. As time progress, the charged zones continuously gain more velocity. However, within the same time interval, the bipolaron gains significantly less velocity than the polaron. In addition, the bipolaron reaches its terminal velocity regime while the polaron is still building momentum. We attribute this disparity as a consequence of the additional distortion stress that the bipolaron puts in the lattice. Moreover, increasing the electric field strength enforces a more intense velocity gain regime.

Recently, our group reported an alternative charge transport description that accounts directly for the quasiparticles motion [32]. As discussed in the methodology section, the model treats their dynamics as the motion of a projectile subjected to Stoke's drag. The yellow lines are the results of fitting the function of Equation 12. One can notice

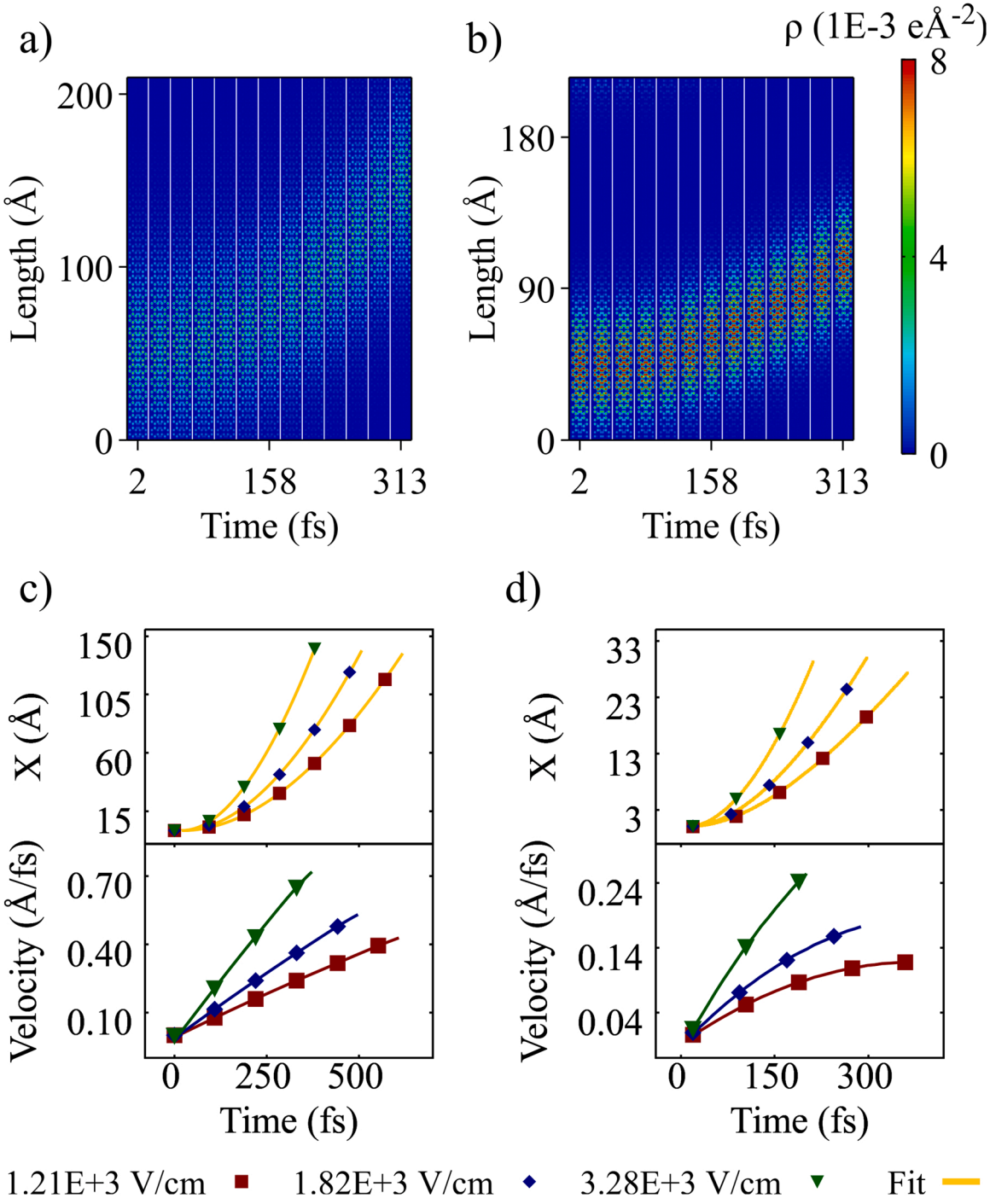

Fig. 3. Charge transport via polarons and bipolarons in the 4-CGNR. (a) and (b) exhibit the time evolution of charged states of Fig. 2 for $E_0 = 3.28 \times 10^3$ V cm^{-1}. Hot colors represent the accumulation of charges, while cold colors depict the inverse. The polaron is represented in (a), while the bipolaron in (b). The former and the latter dynamical evolution are placed in (c) and (d), respectively. Red, blue and green points/lines represent dynamics with $E_0 = 1.21 \times 10^3$, 1.82×10^3, and 3.28×10^3 V cm^{-1}, respectively. The yellow line in the position plots is the fitting of the trajectory.

agreement between data and fit, reinforcing the approach's reliability. The numerical data regarding the fitted coefficients can be found in the supplementary information file.

Fig. 4 shows the mobility as a function of the electric field for the two quasiparticles. We estimate the values based on the steady-current model described in the Methodology section. The red and blue lines are guidelines for polaron and bipolaron data, respectively. The profile of each carrier is intrinsically distinct. As the field grows, polaron's mobility tends to decay. Inversely, in the bipolaron case, mobility continuously increases. The trend of the former quasiparticle is a result of phonon collisions. As E_0 grows, the carry becomes more and more mobile. That allows it to encounter phonons previously emitted. Polarons present a lighter lattice deformation amplitude due to their moderate charge. Because of that, the vibrational disturbance has the potential to disarray the very quasiparticle. Collisions diminish transport efficiency, leading to mobility decay. SSH-based simulations for the polyacetylene (PA) point to similar outcomes [42]. In that system, higher electric fields accelerate more the polarized regions [41]. The lattice reacts by manifesting a more powerful vibrational disorder. Ultimately, the interaction between phonons and the polaron translates

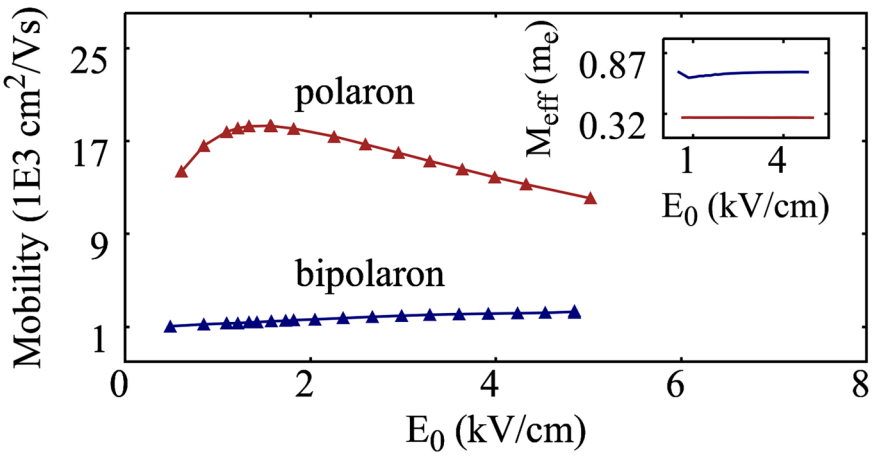

Fig. 4. Transport response of polaron and bipolaron under the electric field strength (E_0). The red and blue triangles assign simulations in which the mobility of polaron and bipolaron are probed. The colored lines are guidelines. Following the same color representation, the inset displays the respective effective masses of each carrier as E_0 changes.

into a sensible change in the quasiparticle amplitude distortion.

One can notice a peak for fields around 1–2 kV/cm. In this electric field range, the polaron drifts smoothly, experiencing no phonon-related dissipating effects. We consider that there are possibly two causes for this regime. The first possible cause is that, within this range, the scattered phonons do not possess enough momentum to disrupt the quasiparticle. The other cause is that the polarized region gained insufficient impulse to reach scattered phonons [40,43]. Therefore, collision effects do not occur substantially. As a result, increasing the electric field can only enforce further mobilization. The estimated polaron mobility extends through the range 12,069–18,312 cm^2/Vs. The magnitude is considerably lower than the one found in pure graphene, which is estimated to reach up to 200,000 cm^2/Vs [7,8]. That sharp difference arises because these materials can have dramatically different topological phases. Graphene allows massless carriers around the so-called Dirac points [2,6]. That feature translates into its outstanding mobility. However, the same does not occur in semiconducting GNRs [9,12,44,45]. Depending on the edge shape, narrow nanoribbons can display a finite energy bandgap due to lateral confinement effects. As a result, the charge carriers will have a non-zero effective mass. The existence of this transport inertia diminishes the potential to carry charges alongside the material. Ultimately, mobility suffers a substantial drop [46,47].

Nonetheless, our estimated mobility measure reveals the carrier as significantly more mobile than observed in other GNRs. Previous experimental works report mixed GNRs sub-10-nm wide with mobility of about 200 cm^2/Vs [48,49] and 1500 cm^2/Vs for 14 nm wide specimens [50,51]. More recently, Terahertz spectroscopy measures point out 9-AGNR to have a mobility of about 350 cm^2/Vs. Moreover, theoretical simulations predict AGNRs being even more mobile if they are sufficiently wide [52,53]. However, due to reduced confinement effects, the mobility gain comes at the expense of the gap magnitude. Significant wide AGNRs such as 34-AGNR may have electron mobility of about 40,000 cm^2/Vs [7] but their gaps are as narrow as about 0.5 eV. This inverse relationship between gap and mobility limits the applicability of such materials. That said, our findings reveal the CGNR superior performance, even if compared with wide AGNRs. Both materials present similar mobility. However, 4-CGNR's gap is about 3x greater. That better balancing between gap and mobility enforces the suitability of this nanoribbon for future applications.

CGNRs also present another transport advantage if compared with AGNRs. As well known, the energy bandgap profile of the latter has a non-smooth dependence with width changes[9,44]. As discussed previously, the gap magnitude directly influences the effective mass. Therefore, the non-smooth relationship extends to the transport inertia as well. Ultimately, mobility suffers from the same constrain. Just like the gap or the effective mass, mobility also has a non-smooth response over width changes. This condition alone can bring limitations in the development of future devices. For instance, mobility of 34, 35, and 36-AGNR are estimated in 40,000, 2500, and 20,000 cm^2/Vs [7,8]. On the other hand, cove-type GNRs allow smooth gap tune [11]. Then, unlike the AGNRs, these nanoribbons might sustain a mobility tune process more direct.

Bipolaron's regime resembles the one experienced by the polaron in low fields. However, its origin comes from another effect. Like in the previous case, the range of E is not strong enough to cause phonon collision. Thus, increasing it can only mobilize more the charge carriers. However, we do not expect profile changes even when the simulated interval is sufficient to enable phonon impacts. The reason for that is directly related to bipolaron's charge. Its additional charge inducts a higher lattice distortion. Thus, vibrational disturbances are not strong enough to muddle the quasiparticle lattice amplitude. As can be seen, the mobility gain here is way more modest when compared to the polaron case. That happens because bipolarons put a higher degree of distortion on the lattice, along with a more intense charge accumulation. Mobilize such polarized regions is more expensive energetically, leading to a generalized mobility loss. Bipolaron's mobility values lie within the range of 1051–2233 cm^2/Vs. This magnitude is significantly lower than the observed in polaron. However, even this carrier still shows better performance than found in other GNR types, as discussed previously.

The inset in Figure 4 shows the quasiparticle mean effective mass as a function of the electric field. The red and blue lines represent, respectively, the polaron and the bipolaron. As can be seen, the obtained values are essentially field-independent. We estimate polaron's and bipolaron's effective masses, in units of free electron mass (m_e), at 0.285 and 0.682, respectively. This result is expected since the latter quasiparticle comes from a more intense lattice deformation and charge accumulation, translating into greater transport inertia.

The above results can be compared with several previous theoretical works. A theoretical investigation using the BTE estimated hole and electron mobilities in the 4CGNR to be 472 and 18,700 cm^2/Vs, respectively [28]. As it can be seen, the obtained electron mobility matches very well our estimates for polarons, whereas hole mobilities appear to be closer to our results for bipolarons. These similarities are surprising considering the fact that the BTE model accounts only for existence of acoustic phonons, which we expect to affect predictions for GNRs [54].

When it comes to comparing effective masses, a previous work calculated hole and electron effective masses to be 0.228 m_e and 0.246 m_e, respectively [28], which agrees well with our above estimates for the

effective mass of polarons. Furthermore, our calculated values are similar to previous results obtained for AGNRs. For instance, we have estimated the polaron effective mass in 9-AGNR to be roughly 0.31 m_e. In contrast, the bipolaron's effective mass in 9-AGNR varies between 4 and 6 m_e [32], an order of magnitude larger than those found in 4-CGNR. The difference results from the structural arrangement of the latter GNR. Cove edges can be seen as the superposition of armchair, and zig-zag borders [11]. ZGNRs, like graphene, present no lattice symmetry break. As a result, their charge carriers are essentially massless. Then, to some extent, the edge mixing in CGNRs absorbs this attribute, enabling lighter carriers than the ones found in GNRs with pure armchair edges. This result supports the role of 4-CGNR as a possible host to highly efficient charge carriers.

The panel in Fig. 5 gathers additional transport-related measures. Fig. 5(a) displays the estimated current-voltage profiles of the polaron and bipolaron. In Fig. 5(b) we present B of each carrier as a function of the electric field strength. In both figures, red and blue curves refer to polaron and bipolaron, respectively. Here, we estimate the current by assuming a steady charge flow of carriers in terminal velocity. A closer look at the curves reveals distinct responses. The polaron case consists of two different regimes. For low potentials, around 1–30 mV, the current increases almost linearly. However, it starts to reach some saturation value as the potential grows further. That behavior is due to collision effects. Higher field values induce greater acceleration to the carriers. However, at some point, the quasiparticles become mobile enough to meet scattered phonons. The encounter between the structures limits the charge transport efficiency. Once a nanoribbon fully populated by polarons reaches this saturation state, further potential difference, V, increment will likely cause minimal current variation.

On the other hand, the bipolaron case behaves differently. Here, aside from an initial potential range, the I-V curve is almost linear. Once again, we can relate the interplay between the quasiparticle and phonons with the transport profile. The phonon collisions are not able to significantly influence the bipolaron's motion. Thus, increasing the potential will only deliver more impulse to the polarized region. The amount of charge transported increases, translating into a current gain. We emphasize that, although polarons have mobility considerably greater than bipolarons, their contribution to the I-V curve is similar. Moreover, the bipolaron's crescent profile suggests that, given sufficient potential, it may even overcome polaron's current. Finally, the distinguished transport behavior of the quasiparticles in Fig. 5(a) signs their intrinsic properties. The 4-CGNR deliver a more efficient charge transport than previous GNRs types.

The magnitude of the frictional coefficient allows us to extend the quasiparticle characterization process. In Fig. 5(b), one can observe two different profiles for the polaron. As E_0 increases, the curve shows a non-monotonic shape. B decays for electric fields in the 0–2 kV/cm range. For higher field intensities, B starts to increase. Once again, the curve shape

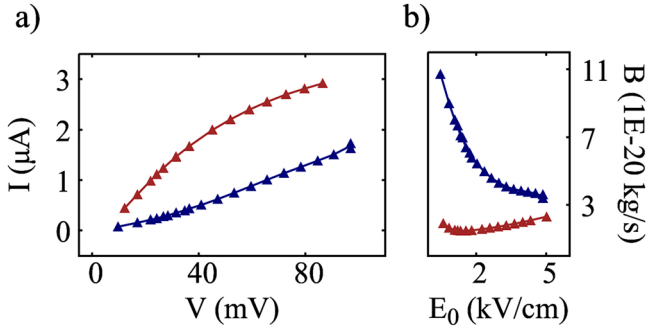

Fig. 5. Transport profile of the charge carriers. (a) shows the I-V curve of both quasiparticles. Red and blue colors designate the polaron and bipolaron, respectively. Additionally, (b) shows the dependency between the dissipation coefficient (B) with the electric field strength.

can be related to the occurrence of phonon collisions. This effect is the source of restraint. Therefore, the dissipation coefficient directly relates to the impact of the collisions. In that sense, the brief B decay trend results from quasiparticle mobilization with a negligible influence of disseminated phonons. As much E_0 increases, the lattice does not present greater resistance to motion. Correlative analysis fits the other field regime. When the field increases, the quasiparticle faces enough phonons to reduce its mobility. That translates into a B gain trend.

Conversely, bipolaron shows a consistent monotonic B decay. Such response directly connects with how the polarized structure interacts with phonons. As discussed in Fig. 4, bipolaron's existence provokes a more prominent localized lattice distortion. Unlike in the polaron case, the phonon interplay does not produce significant interference on that structure. Thus, in other words, bipolaron motion does not endure additional resistance due to vibrational effects. Since this is the only restrain accounted for, higher electric fields can only facilitate charge translation. As an effect, B decreases continuously.

The profile of B over electric field strength corroborates the previous mobility analysis. The intrinsic relationship of this dissipation coefficient sheds light on the lattice response led by scattered phonons. Results clearly distinguish polaron and bipolaron cases due to their interaction with such vibrational effects. As the field increases, the former quasiparticle suffers major lattice restraints, while the latter shows no visible interference. Thus, if such a trend maintains for more intense fields, bipolarons could overcome polaron transport efficiency.

4. Conclusion

In conclusion, we investigated the charge transport of the 4-CGNR by explicitly considering the quasiparticle mechanism. The nanoribbon was simulated employing a 2-D extended SSH model with electron-phonon coupling. Stationary solutions revealed the existence of at least two charged quasiparticles, namely polaron, and bipolaron. Then, we proceeded to probe dynamical transport characteristics of each carrier. Findings unveiled the existence of a distinctive transport regime for each quasiparticle. Polaron's mobility ranges between 12,069 and 18,312 cm^2/Vs, while bipolaron lies around 1051–2233 cm^2/Vs for a same electric field strength variation. Further analysis linked the distinctive regimes with the interplay of the quasiparticles with scattered phonons. We found that a light carrier, such as the polaron, is severely affected by phonon collision in high fields. On the other hand, bipolaron experienced no interference, regardless of the phonon's momentum.

Additionally, both carriers show impressive mobility if compared with previously studied GNRs. They also present modest effective masses. We estimated polaron's and bipolaron's as, respectively, 0.285 and 0.682 m_e. These quantities showed no apparent variation for E_0 within 0.5–5 kV. All these traits confer the 4-CGNR's carriers a great latent potential for future devices. Finally, we presented two alternative transport measurements that contribute to further characterize these carriers.

CRediT authorship contribution statement

Tiago Cassiano: Conceptualization, Methodology, Software, Validation, Formal analysis, Investigation, Writing – original draft, Visualization. **Leonardo Evaristo**: Conceptualization, Validation, Formal analysis, Investigation, Writing – review & editing. **Luiz Ribeiro**: Conceptualization, Formal analysis, Investigation, Writing – review & editing. **Geraldo Magela**: Conceptualization, Methodology, Software, Validation, Formal analysis, Investigation, Writing – review & editing, Visualization. **Pedro Neto**: Conceptualization, Methodology, Software, Validation, Formal analysis, Investigation, Writing – review & editing, Visualization, Supervision.

Declaration of Competing Interest

The authors declare that they have no known competing financial interests or personal relationships that could have appeared to influence the work reported in this paper.

Acknowledgments

The authors gratefully acknowledge the financial support from Brazilian Research Councils CNPq, (grant. number 304637/2018–1) CAPES, and FAPDF. P.H.O.N, and G.M.S. gratefully acknowledge, respectively, the financial support from FAPDF grants 0193.001662/2017, and 0193.001766/2017. G.M.S. gratefully acknowledges the financial support from CNPq grants 304637/2018–1. L.E.S. acknowledges support by a research grant (00028053) from VILLUM FONDEN.

Appendix A. Supporting information

Supplementary data associated with this article can be found in the online version at doi:10.1016/j.synthmet.2022.117056.

References

[1] K.S. Novoselov, A.K. Geim, S.V. Morozov, D. Jiang, Y. Zhang, S.V. Dubonos, I. V. Grigorieva, A.A. Firsov, Electric field effect in atomically thin carbon films, Science 306 (2004) 666.
[2] A.C. Neto, F. Guinea, N.M. Peres, K.S. Novoselov, A.K. Geim, The electronic properties of graphene, Rev. Mod. Phys. 81 (2009) 109.
[3] C. Chung, Y.-K. Kim, D. Shin, S.-R. Ryoo, B.H. Hong, D.-H. Min, Biomedical applications of graphene and graphene oxide, Acc. Chem. Res. 46 (2013) 2211.
[4] P. Avouris, F. Xia, Graphene applications in electronics and photonics, Mrs Bull. 37 (2012) 1225.
[5] K.M. Shahil, A.A. Balandin, Thermal properties of graphene and multilayer graphene: Applications in thermal interface materials, Solid State Commun. 152 (2012) 1331.
[6] A.K. Geim, K.S. Novoselov, The rise of graphene, in Nanoscience and technology, World Sci. (2010) 11–19.
[7] G. Wang, Effect of edge-hydrogen passivation and saturation on the carrier mobility of armchair graphene nanoribbons, Chem. Phys. Lett. 533 (2012) 74.
[8] K.I. Bolotin, K.J. Sikes, Z. Jiang, M. Klima, G. Fudenberg, J. e. Hone, P. Kim, H. Stormer, Ultrahigh electron mobility in suspended graphene, Solid State Commun. 146 (2008) 351.
[9] Y.-W. Son, M.L. Cohen, S.G. Louie, Energy gaps in graphene nanoribbons, Phys. Rev. Lett. 97 (2006), 216803.
[10] L. Yang, M.L. Cohen, S.G. Louie, Excitonic effects in the optical spectra of graphene nanoribbons, Nano Lett. 7 (2007) 3112.
[11] T.S.A. Cassiano, F.F. Monteiro, L.E. de Sousa, G.M. e Silva, P.H. de Oliveira Neto, Smooth gap tuning strategy for cove-type graphene nanoribbons, RSC Adv. 10 (2020) 26937.
[12] D.J. Rizzo, G. Veber, T. Cao, C. Bronner, T. Chen, F. Zhao, H. Rodriguez, S.G. Louie, M.F. Crommie, F.R. Fischer, Topological band engineering of graphene nanoribbons, Nature 560 (2018) 204.
[13] A. Narita, X. Feng, Y. Hernandez, S.A. Jensen, M. Bonn, H. Yang, I.A. Verzhbitskiy, C. Casiraghi, M.R. Hansen, A.H. Koch, et al., Synthesis of structurally well-defined and liquid-phase-processable graphene nanoribbons, Nat. Chem. 6 (2014) 126.
[14] C. Liu, J. Zhang, M. Muruganathan, H. Mizuta, Y. Oshima, X. Zhang, Origin of nonlinear current-voltage curves for suspended zigzag edge graphene nanoribbons, Carbon 165 (2020) 476.
[15] A. Kimouche, M.M. Ervasti, R. Drost, S. Halonen, A. Harju, P.M. Joensuu, J. Sainio, P. Liljeroth, Ultra-narrow metallic armchair graphene nanoribbons, Nat. Commun. 6 (2015) 1.
[16] L. Ma, J. Wang, F. Ding, Recent progress and challenges in graphene nanoribbon synthesis, ChemPhysChem 14 (2013) 47.
[17] J.L. Bredas, G.B. Street, Polarons, bipolarons, and solitons in conducting polymers, Acc. Chem. Res. 18 (1985) 309.
[18] W.F. daCunha, P.H. Acioli, P.H. de Oliveira Neto, R. Gargano, G.M. e Silva, Polaron properties in armchair graphene nanoribbons, J. Phys. Chem. A 120 (2016) 4893.
[19] P.H. de Oliveira Neto, T. Van Voorhis, Dynamics of charge quasiparticles generation in armchair graphene nanoribbons, Carbon 132 (2018) 352.
[20] M.L.P. Júnior, B.G.E. Neto, W.F. Giozza, R.T.S. Júnior, G.M. e Silva, L.A.R. Júnior, Transport of quasiparticles in coronene-based graphene nanoribbons, J. Mater. Chem. C. 8 (2020) 12100.
[21] M.M. Fischer, L.A.R. Junior, W.F. da Cunha, L.E. de Sousa, G.M. e Silva, P.H. de Oliveira Neto, Ultrafast direct generation of quasiparticles in graphene nanoribbons, Carbon 158 (2020) 553.
[22] M.L.P. Júnior, P.H. de Oliveira Neto, D.A. daSilvaFilho, L.E. de Sousa, G.M. e Silva, L.A.R. Júnior, Charge localization and hopping in a topologically engineered graphene nanoribbon, Sci. Rep. 11 (2021) 1.
[23] D.A. Areshkin, B.K. Nikolić, Electron density and transport in top-gated graphene nanoribbon devices: First-principles green function algorithms for systems containing a large number of atoms, Phys. Rev. B 81 (2010), 155450.
[24] G.G. Silva, L.A.R. Junior, M.L.P. Junior, A.L. de Almeida Fonseca, R.T. de Sousa Júnior, G.M. e Silva, Bipolaron dynamics in graphene nanoribbons, Sci. Rep. 9 (2019) 1.
[25] R. Shishir, D. Ferry, and S. Goodnick, Room temperature velocity saturation in intrinsic graphene,in Journal of Physics:Conference Series, 193 (IOP Publishing, 2009: 012118.
[26] S. Bruzzone, G. Fiori, Ab-initio simulations of deformation potentials and electron mobility in chemically modified graphene and two-dimensional hexagonal boron-nitride, Appl. Phys. Lett. 99 (2011), 222108.
[27] N. Amin, M.T. Ahmadi, Z. Johari, J. Webb, S. Mousavi, and R. Ismail, Drift velocity and mobility of a graphene nanoribbon in a high magnitude electric field, in AIP Conference Proceedings, vol. 1337 (American Institute of Physics, 2011: 177–179.
[28] I. Ivanov, Y. Hu, S. Osella, U. Beser, H.I. Wang, D. Beljonne, A. Narita, K. Müllen, D. Turchinovich, M. Bonn, Role of edge engineering in photoconductivity of graphene nanoribbons, J. Am. Chem. Soc. 139 (2017) 7982.
[29] N. Smith, Classical generalization of the drude formula for the optical conductivity, Phys. Rev. B 64 (2001), 155106.
[30] T.L. Cocker, D. Baillie, M. Buruma, L.V. Titova, R.D. Sydora, F. Marsiglio, F. A. Hegmann, Microscopic origin of the drude-smith model, Phys. Rev. B 96 (2017), 205439.
[31] R. Lovrinčić, A. Pucci, Infrared optical properties of chromium nanoscale films with a phase transition, Phys. Rev. B 80 (2009), 205404.
[32] M.M. Fischer, L.E. de Sousa, L.L. e Castro, L.A. Ribeiro, R.T. de Sousa, G.M. e Silva, P.H. de Oliveira Neto, Effective mass of quasiparticles in armchair graphene nanoribbons, Sci. Rep. 9 (2019) 1.
[33] W. Su, J. Schrieffer, A.J. Heeger, Solitons in polyacetylene, Phys. Rev. Lett. 42 (1698) (1979).
[34] G.G. Silva, W.F. daCunha, R.T. de Sousa Junior, A.L.A. Fonseca, L.A.R. Júnior, G. M. e Silva, Influence of quasi-particle density over polaron mobility in armchair graphene nanoribbons, Phys. Chem. Chem. Phys. 20 (2018) 16712.
[35] W.F. daCunha, L.A.R. Junior, A.L. de Almeida Fonseca, R. Gargano, G.M. e Silva, Impurity effects on polaron dynamics in graphene nanoribbons, Carbon 91 (2015) 171.
[36] W.F. daCunha, P.H. de Oliveira Neto, A. Terai, G.M. e Silva, Dynamics of charge carriers on hexagonal nanoribbons with vacancy defects, Phys. Rev. B 94 (2016), 014301.
[37] V.N. Kotov, B. Uchoa, V.M. Pereira, F. Guinea, A.C. Neto, Electron-electron interactions in graphene: Current status and perspectives, Rev. Mod. Phys. 84 (2012) 1067.
[38] C. Lee, X. Wei, J.W. Kysar, J. Hone, Measurement of the elastic properties and intrinsic strength of monolayer graphene, science 321 (2008) 385.
[39] P.H. De Oliveira Neto, J.F. Teixeira, W.F. DaCunha, R. Gargano, G.M. E. Silva, Electron-lattice coupling in armchair graphene nanoribbons, J. Phys. Chem. Lett. 3 (2012) 3039.
[40] A.V.P. Abreu, L.A.R. Junior, G.G. Silva, M.L.P. Junior, B.G. Enders, A.L.A. Fonseca, G.M. e Silva, Stability conditions of armchair graphene nanoribbon bipolarons, J. Mol. Model. 25 (2019) 1.
[41] A.A. Johansson, S. Stafström, Nonadiabatic simulations of polaron dynamics, Phys. Rev. B 69 (2004), 235205.
[42] T. Astakhova, G. Vinogradov, New aspects of polaron dynamics in electric field, Eur. Phys. J. B 92 (2019) 1.
[43] L.A.R. Junior, S. Stafström, Polaron stability in molecular semiconductors: Theoretical insight into the impact of the temperature, Electr. Field Syst. Dimens., Phys. Chem. Chem. Phys. 17 (2015) 8973.
[44] L. Yang, C.-H. Park, Y.-W. Son, M.L. Cohen, S.G. Louie, Quasiparticle energies and band gaps in graphene nanoribbons, Phys. Rev. Lett. 99 (2007), 186801.
[45] A. Narita, I.A. Verzhbitskiy, W. Frederickx, K.S. Mali, S.A. Jensen, M.R. Hansen, M. Bonn, S. De Feyter, C. Casiraghi, X. Feng, et al., Bottom-up synthesis of liquid-phase-processable graphene nanoribbons with near-infrared absorption, ACS Nano 8 (2014) 11622.
[46] A. Narita, X. Feng, Y. Hernandez, S.A. Jensen, M. Bonn, H. Yang, I.A. Verzhbitskiy, C. Casiraghi, M.R. Hansen, A.H. Koch, G. Fytas, O. Ivasenko, B. Li, K.S. Mali, T. Balandina, S. Mahesh, S. De Feyter, K. Müllen, Synthesis of structurally well-defined and liquid-phase-processable graphene nanoribbons, Nat. Chem. 6 (2014) 126.
[47] Y. Yang, R. Murali, Impact of size effect on graphene nanoribbon transport, IEEE Electron Device Lett. 31 (2010) 237.
[48] X. Li, X. Wang, L. Zhang, S. Lee, H. Dai, Chemically derived, ultrasmooth graphene nanoribbon semiconductors, science 319 (2008) 1229.
[49] X. Wang, Y. Ouyang, X. Li, H. Wang, J. Guo, H. Dai, Room-temperature all-semiconducting sub-10-nm graphene nanoribbon field-effect transistors, Phys. Rev. Lett. 100 (2008), 206803.
[50] L. Jiao, X. Wang, G. Diankov, H. Wang, H. Dai, Facile synthesis of high-quality graphene nanoribbons, Nat. Nanotechnol. 5 (2010) 321.
[51] F. Schwierz, Graphene transistors, Nat. Nanotechnol. 5 (2010) 487.
[52] H. Raza, E.C. Kan, Armchair graphene nanoribbons: Electronic structure and electric-field modulation, Phys. Rev. B 77 (2008), 245434.
[53] M.-Q. Long, L. Tang, D. Wang, L. Wang, Z. Shuai, Theoretical predictions of size-dependent carrier mobility and polarity in graphene, J. Am. Chem. Soc. 131 (2009) 17728.
[54] T. Fang, A. Konar, H. Xing, D. Jena, Mobility in semiconducting graphene nanoribbons: Phonon, impurity, and edge roughness scattering, Phys. Rev. B 78 (2008), 205403.